INTERNATIONAL JOURNAL FOR NUMERICAL METHODS IN FLUIDS
Int. J. Numer. Meth. Fluids (2007)
Published online in Wiley InterScience (www.interscience.wiley.com). DOI: 10.1002/fld.1651

Height functions for applying contact angles to 2D VOF simulations

S. Afkhami and M. Bussmann*, †

Department of Mechanical and Industrial Engineering, University of Toronto, Toronto, Ont., Canada

SUMMARY

Recent work on a consistent representation of surface tension and on the accurate computation of interface curvature has extended the applicability of the volume-of-fluid, or VOF, method to surface tension-driven phenomena. We have extended these methodologies to interfaces near solid surfaces; specifically, we show how height functions can be used to enforce a contact angle boundary condition at a contact line, for the full range of contact angles. As such, this work may be viewed as following up on the methodology of Renardy *et al*. (*J. Comput. Phys*. 2001; **171**:243–263). This approach yields accurate values of curvature and the surface tension force at contact lines, values that converge with mesh refinement. The efficacy of the methodology is demonstrated using 2D examples of static fluid configurations in equilibrium and dynamic contact line phenomena that approach known equilibrium configurations. Copyright © 2007 John Wiley & Sons, Ltd.

Received 27 May 2007; Revised 26 September 2007; Accepted 27 September 2007

KEY WORDS: volume of fluid; VOF; contact angle; contact line; height function

1. INTRODUCTION

Numerous methods have been devised for the simulation of interface kinematics. Among these, the volume-of-fluid, or VOF, method is widely used for interfacial flow simulations because of its relative simplicity and volume conservation properties. Until recently, however, the method has not been regarded as appropriate for the study of surface tension-driven phenomena. However, recent improvements to calculating curvature κ and applying the surface tension force appear to resolve this issue [1–5].

*Correspondence to: M. Bussmann, Department of Mechanical and Industrial Engineering, University of Toronto, 5 King's College Road, Toronto, Ont., Canada M5S 3G8.
†E-mail: bussmann@mie.utoronto.ca

These developments have yet to be extended to problems that involve contact lines, the lines that form at the intersection of a fluid–fluid interface and a solid surface, as appear in phenomena that involve, for example, sessile droplets and coatings. The focus of this paper, then, is the extension of these methodology developments to contact lines, and as such, follows up on the work of Renardy *et al*. [6] on a VOF approach to modelling 2D contact line phenomena based on an earlier (and less accurate) approach to treating surface tension.

The common approach to modelling surface tension in VOF simulations is the continuum surface force (CSF) method of Brackbill *et al*. [7], which treats surface tension as a volumetric force acting on fluid near an interface. In a subsequent paper, Kothe and Mjolsness [8] demonstrated the use of CSF in the RIPPLE code and introduced the idea of reorienting interface normals at cell vertices along a solid boundary to reflect a known contact angle; these reoriented normals then affected both the orientation of neighbouring VOF reconstructions as well as the calculation of local curvatures. This approach to applying a contact angle was subsequently utilized by various authors (e.g. [9–11]) in numerical studies of contact line phenomena.

As recent studies [1–5] have shown, older methodologies for applying surface tension in VOF codes and for calculating normals and curvatures from volume fractions yield results that do not converge with mesh refinement, and the resulting flows can be plagued by so-called spurious or parasitic currents—aphysical velocities induced solely by discretization errors [12, 13]. In these older methods (e.g. [7, 8, 14]), unit normals $\hat{n} = \nabla f / |\nabla f|$ and curvatures $\kappa = -\nabla \cdot \hat{n}$ are obtained from the gradient of the volume fraction field or a smoothed version of the same. Such gradient-based methods of calculating normals and curvatures have largely given way to what may be termed 'integral' methods, in which these quantities are evaluated by various geometric means [1, 3, 4, 15]; these are methods that clearly yield more accurate results when interfaces are reasonably well resolved. It is the height function (HF) method [1, 3] that we consider here.

The application of HFs to contact lines is not entirely new. Recent work on the development of a VOF-based code for modelling wave impact [16] and liquid sloshing [17] phenomena includes an approach to treating contact lines that is in some ways similar to that presented here, albeit implemented in an entirely different type of flow code (a single fluid calculation, a VOF methodology based on that of Hirt and Nichols [18], and surface tension incorporated as a boundary condition to the pressure solve, rather than as a CSF volumetric force). Furthermore, this work [16, 17] is not about contact lines *per se*; hence, there is little analysis of the methodology.

Our code is an extension of an early version of the 'Gerris' code of Popinet [19, 20] for the solution of the incompressible Euler equations. We implemented surface tension and multi-fluid viscosity models into the code, and then used that as the basis for developing the 2D HF-based contact line VOF methodology presented here.

In this paper, we present the methodology and the results of various tests. We briefly examine the errors in normals and curvatures for a semicircular drop initialized exactly, and demonstrate the convergence with mesh refinement that is not obtained when calculating normals and curvatures *via* gradient-based methods. We then consider the behaviour of drops in equilibrium, by examining the magnitude of induced spurious currents and the associated errors in volume fractions, for contact angles that range from 30 to 150°. Finally, we consider contact line-driven flows, as a drop initially in equilibrium is driven by a sudden change in the contact angle, and assess the results by examining the equilibrium shapes that result.

DOI: 10.1002/fld

2. METHODOLOGY

2.1. Overview

The Navier–Stokes equations govern an incompressible two-phase flow:

$$\partial U/\partial t+\nabla\cdot(UU)=-\frac{1}{\rho}(\nabla p+\nabla\cdot(\mu(\nabla U+\nabla U^{\mathrm{T}}))+F_{\mathrm{st}}+F_{\mathrm{b}}) \tag{1}$$

where U is the velocity, p the pressure, ρ the density, μ the viscosity, F_{st} the volumetric surface tension force, and F_{b} represents any other body forces acting on the fluid. Each fluid is considered to be incompressible; hence the continuity equation

$$\nabla\cdot U=0 \tag{2}$$

is valid throughout the domain.

For a two-fluid system, a characteristic function f ($=0$ in a fluid 1 and $=1$ in fluid 2) is used to track fluid volume. The advection equation for f is

$$\partial f/\partial t+U\cdot\nabla f=0 \tag{3}$$

Density and viscosity may vary from one fluid to another, but are assumed constant in any particular fluid. These are evaluated using volume-weighted formulae:

$$\rho=\rho_1+(\rho_2-\rho_1)f \tag{4}$$

$$\mu=\mu_1+(\mu_2-\mu_1)f \tag{5}$$

where subscripts 1 and 2 refer to the two-fluid phases, respectively.

We implemented our methodology in an early version of the Gerris software [19, 20] that solves the flow equations *via* an adaptively refined projection method based on a variable-density fractional-step scheme [21]. Variables are collocated at cell centres and advection terms are discretized using a second-order upwind scheme. A face-centred velocity field is exactly projected, and a cell-centred velocity field is approximately projected, onto a divergence-free velocity field, with the pressure field obtained as the solution of a Poisson equation. Since face-centred velocities are divergence free, the function f is advected using these.

The equations are solved on a square mesh that is locally refined by recursively dividing cells that satisfy a given criterion. The criterion used for all results presented in this paper is simply the presence of a fluid interface. Cells are uniformly refined near the interface, in a band wide enough to allow us to implement surface tension methods as on a uniform mesh; away from interfaces, the mesh is typically coarser. In what follows, we refer to the finest level of refinement as Δ.

2.2. The VOF method

In a VOF method, the discrete form of the function f represents the volume fraction of a cell filled with, in this case, fluid 2. Away from the interface, $f=0$ or 1; 'interface cells' correspond to $0<f<1$. Equation (3) is usually solved in two steps: a geometric interface reconstruction, followed by an advection step based on the reconstructed interface. In this work, the reconstruction is a 'piecewise linear interface calculation' (PLIC), followed by a Lagrangian advection step [22].

DOI: 10.1002/fld

In the PLIC step, given the volume fraction in an interface cell and an approximate normal vector, a linear interface is constructed within each cell, corresponding exactly to the normal and the volume fraction. For many years, a common approach (e.g. [8, 14]) has been to calculate the normal $\mathbf{n}=\nabla\tilde{f}$, where $\tilde{f}$ is a smoothed (convolved) version of the volume fraction field f (such an approach is equivalent to calculating ∇f *via* a stencil that is wider than the simple 5-point stencil in 2D).

Unfortunately, such normals do not converge with mesh refinement when the stencil size is fixed [23], and increasing the stencil size with refinement can be prohibitively expensive. One alternative that does yield normals that converge is the HF methodology, which is a variation of the ELVIRA algorithm [15], and the basis for the contact line methodology presented in this paper.

2.3. Surface tension implementation

The CSF model [7] is used to discretize the surface tension force $F_{\mathrm{st}}=\sigma\kappa\delta\hat{n}$ (σ is the surface tension coefficient, δ the Dirac delta function, and $\hat{n}$ a unit interface normal). Until recently, $\delta\hat{n}$ was commonly discretized as $\nabla\tilde{f}$ and curvature was calculated as $\kappa=-\nabla\cdot\hat{n}$, where $\hat{n}=\nabla\tilde{f}/|\nabla\tilde{f}|$. However, this led to two problems: (i) the development of spurious currents, the magnitude of which could overwhelm any real velocities in some problems; and (ii) very poor estimates of curvature that in fact worsened with mesh refinement [1] when $\nabla\tilde{f}$ was calculated from a fixed stencil.

Our methodology addresses both issues. First, recent work [3, 4] demonstrates that F_{st} should be discretized in a way that is consistent with the discretization of ∇p, so that for the simple case of a static drop with exactly prescribed curvature, the surface tension induces the exact jump in pressure $\sigma\kappa$ and induces no spurious currents [13]. Second, methods are now available [1, 4] to calculate curvatures from volume fractions that converge with mesh refinement; HFs are one such method, that we utilize in this work.

We now briefly present our implementation of CSF in the Gerris flow solver. Following the fractional-step projection method [21], Equation (1) is decomposed into predictor and corrector steps:

$$\frac{U^{**}-U^{n}}{\Delta t}=-[\nabla\cdot(UU)]^{n+1/2}+\frac{1}{\rho^{n+1}}\nabla\cdot(\mu^{n}(\nabla U+\nabla U^{\mathrm{T}})^{n})+\frac{1}{\rho^{n+1}}F_{\mathrm{st}}^{n+1} \tag{6}$$

$$\frac{U^{n+1}-U^{**}}{\Delta t}=-\frac{1}{\rho^{n+1}}\nabla p^{n+1} \tag{7}$$

where $\Delta t=t^{n+1}-t^{n}$ and U^{**} represents an intermediate velocity. For simplicity, we ignore the convective and viscous terms in what follows and present only the treatment of the surface tension term. The intermediate velocity in Equation (6) is computed as

$$U_{\mathrm{cc}}^{**}=U_{\mathrm{cc}}^{n}+\Delta t\left(\left(\frac{1}{\rho}F_{\mathrm{st}}\right)_{\mathrm{fc}}^{n+1}\right)_{\mathrm{f}\to\mathrm{c}} \tag{8}$$

where the subscripts cc and fc denote cell-centred and face-centred quantities, and $\mathrm{f}\to\mathrm{c}$ refers to the cell-centred averaging of face-centred values. Since we discretize ∇p at faces with a simple

DOI: 10.1002/fld

5-point stencil, a consistent F_{st} must have the following form:

$$(F_{st})_{fc} = (\sigma\kappa\nabla f)_{fc} \tag{9}$$

The intermediate velocities U^{**} are not divergence free. Taking the divergence of Equation (7) and imposing $\nabla \cdot U^{n+1} = 0$ yields a Poisson equation for the pressure:

$$\nabla \cdot \left(\frac{1}{\rho}\nabla p\right)_{cc}^{n+1} = \frac{1}{\Delta t}\nabla \cdot U_{fc}^{**} \tag{10}$$

where U_{fc}^{**} is evaluated as

$$U_{fc}^{**} = \left(U_{cc}^{**} - \Delta t\left(\left(\frac{1}{\rho}F_{st}\right)_{fc}^{n+1}\right)_{f\to c}\right)_{c\to f} + \Delta t\left(\frac{1}{\rho}F_{st}\right)_{fc}^{n+1} \tag{11}$$

and $c \to f$ denotes the face-centred averaging of cell-centred values. Equation (10) is then solved for pressure p_{cc}^{n+1}, and the cell-centred and face-centred velocities are updated as

$$U_{cc}^{n+1} = U_{cc}^{**} - \Delta t\left(\left(\frac{1}{\rho}\nabla p\right)_{fc}^{n+1}\right)_{f\to c} \tag{12}$$

$$U_{fc}^{n+1} = U_{fc}^{**} - \Delta t\left(\frac{1}{\rho}\nabla p\right)_{fc}^{n+1} \tag{13}$$

Although the algorithm involves the averaging of quantities between cell faces and centres, it nevertheless is a sharp methodology that yields only surface tension-induced velocities at faces at which ∇f is non-zero. More importantly, with this consistent implementation of CSF, if one prescribes exact curvatures to a fluid configuration in equilibrium (e.g. static drop), the surface tension force will exactly balance the pressure jump, whether the drop is isolated within another fluid or is a sessile drop resting on a solid surface. This then implies that the accuracy of the surface tension calculation at the contact line rests solely on the accurate evaluation of κ near the solid boundary.

2.4. The HF method

The HF methodology [1, 3, 5] is a technique for calculating interface normals and curvatures from well-resolved volume fraction data, as illustrated in Figure 1. Consider a uniform mesh of size Δ. About each interface cell, in the direction most normal to the interface (estimated here by a simple finite difference evaluation of ∇f [14]), fluid 'heights' are calculated by summing volume fractions. In 2D, we construct either a 7×3 or 3×7 stencil around each interface cell. For example, for the cell (i, j) illustrated in Figure 1, $|n_y| > |n_x|$; hence HFs are constructed by summing volume fractions vertically:

$$h_i = \sum_{k=j-3}^{k=j+3} f_{i,k}\Delta \tag{14}$$

DOI: 10.1002/fld

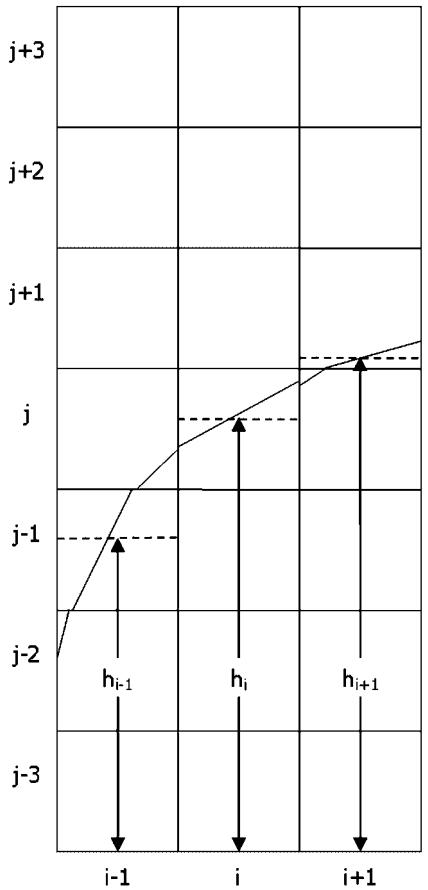

Figure 1. The 7×3 stencil used to calculate fluid heights.

with corresponding expressions for h_{i-1} and h_{i+1}. The heights h are then used to compute the interface normal $\mathbf{n}$ and curvature κ at cell centres:

$$\mathbf{n}_{\mathrm{cc}} = \begin{bmatrix} h_x \\ -1 \end{bmatrix} \tag{15}$$

$$\kappa_{\mathrm{cc}} = \frac{h_{xx}}{(1+h_x^2)^{3/2}} \tag{16}$$

where h_x and h_{xx} are discretized using second-order central differences:

$$h_x = \frac{h_{i+1} - h_{i-1}}{2\Delta} \tag{17}$$

$$h_{xx} = \frac{h_{i+1} - 2h_i + h_{i-1}}{\Delta^2} \tag{18}$$

DOI: 10.1002/fld

Note that for Equation (9) we require face-centred curvatures; these are estimated by simple averaging of the cell-centred values κ_{cc}.

2.5. Contact angle boundary condition

In 2D, a contact line appears as the point at which a fluid–fluid interface meets a solid surface, and for numerical methods that track interfaces, the position of the contact line is exactly known. But here we track the interface implicitly *via* volume fractions; hence, we do not know the precise location of the contact line. Instead, we define a 'contact line cell' as the interface cell along a solid surface that neighbours an empty (for $\theta \leqslant 90°$) or full (for $\theta > 90°$) cell.

The boundary condition to be imposed at the contact line cell is the orientation of the interface, characterized by the contact angle θ (illustrated in Figure 2), the angle between the normal to the interface at the contact line, $\mathbf{n}_{cl}$, and the normal to the solid boundary, $\mathbf{n}_b$. The value of θ affects the numerical methodology in two ways: it defines the orientation $\mathbf{n}$ of the VOF reconstruction in the contact line cell, and it influences the calculation of F_{st} by affecting the calculated curvature.

In order to compute that curvature, we calculate fluid heights horizontally (for $45° \leqslant \theta \leqslant 135°$) or vertically (for $\theta < 45°$ and $\theta > 135°$), as depicted in Figures 3 and 4, respectively. For $45° \leqslant \theta \leqslant 135°$ (Figure 3), we require a height h_0 parallel to the solid surface; h_0 is calculated so that the interface normal $\mathbf{n}$ at the contact line corresponds to $\mathbf{n}_{cl}$:

$$h_0 = h_1 + \Delta / \tan\theta \tag{19}$$

For $\theta < 45°$ and $\theta > 135°$, vertical heights are calculated normal to the solid surface, as illustrated in Figure 4 for the case of $\theta < 45°$; the extension of the methodology to the case of $\theta > 135°$ is straightforward. In order to calculate the individual heights, we require individual values of volume fractions in the so-called 'ghost cells'. We set $f = 1$ in ghost cells beneath the fluid, and we calculate the ghost cell value beneath the contact line by extending the reconstructed interface in the contact line cell into the solid boundary, which then defines all heights except one; for the fluid configuration illustrated in Figure 4, the height h_{i-1} is then calculated as

$$h_{i-1} = h_i - \Delta \tan\theta \tag{20}$$

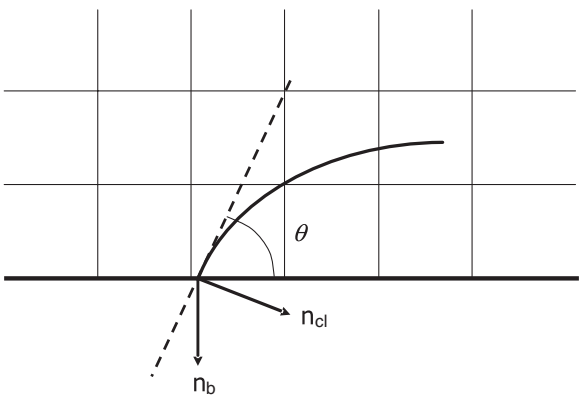

Figure 2. The contact angle θ defines the normal $\mathbf{n}_{cl}$ to the interface at the contact line.

DOI: 10.1002/fld

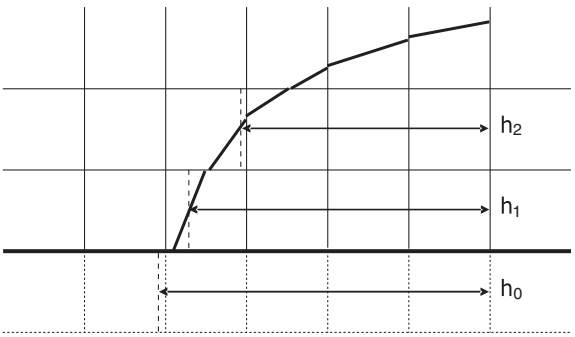

Figure 3. Height functions constructed horizontally, for $45° \leqslant \theta \leqslant 135°$. The height h_0 outside the domain is determined so that the interface slope $\mathbf{n}$ at the contact line corresponds to $\mathbf{n}_{\mathrm{cl}}$.

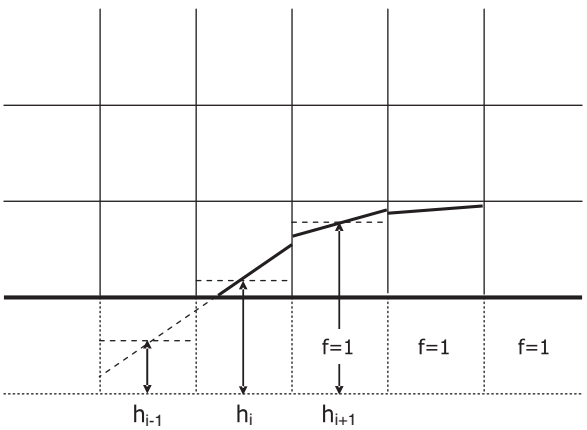

Figure 4. Height functions constructed vertically, for $\theta < 45°$ and $\theta > 135°$. The height h_{i-1} is determined so that the interface slope $\mathbf{n}$ at the contact line corresponds to $\mathbf{n}_{\mathrm{cl}}$.

Finally, it is well known that contact line motion is a mathematical paradox, as the solid surface is a no-slip boundary; as a result, the Navier–Stokes equations yield a stress singularity at the contact line [24]. In order to alleviate that singularity, slip must be introduced [25, 26]; the extent of slip is referred to as the slip length measured normal to the solid boundary. Numerically, the approach to implementing slip depends on the method used to represent the interface. For example, methods that explicitly track an interface (e.g. [27]) require a slip condition for the mesh node at the contact line. On the other hand, most VOF implementations, including ours, utilize cell face normal velocities to advect volume fractions, including those near the contact line. This implies that the methodology includes an implicit slip length $\Delta/2$ along no-slip boundaries.

3. RESULTS

In what follows, we briefly examine the accuracy of normals and curvatures calculated from an exactly initialized volume fraction field; we then examine the behaviour of sessile drops at

DOI: 10.1002/fld

equilibrium; and finally, we present results of drops driven by a sudden change in the specified contact angle.

3.1. HF normals and curvatures

Consider a 2D sessile drop of radius $R=0.25$ centred at the bottom of a 1×1 domain; Figure 5 illustrates the interface and the associated adaptive mesh. At equilibrium, $\theta=90°$, the exact curvature is $1/R$, and the exact normal at any point (x, y) is $(x/y, -1)$, for $-0.5\leqslant x\leqslant 0.5$ and $0\leqslant y\leqslant 1$. The 90° contact angle implies a symmetry boundary condition for the volume fractions; hence, this problem corresponds to a test case of Francois *et al*. [3], who showed that HF curvatures are second-order accurate. Table I presents the L_∞ error for normals (evaluated as the angle between the calculated and exact normals) and curvatures calculated using HFs, and for comparison, the results obtained by calculating $\hat{n}=\nabla\tilde{f}/|\nabla\tilde{f}|$ and $\kappa=-\nabla\cdot\hat{n}$, where the stencil for $\nabla\tilde{f}$ is that of Youngs [14]. The results are dramatic: normals computed from $\nabla\tilde{f}$ remain constant with refinement and curvatures get worse. On the other hand, HF normals are first-order accurate, and curvatures are second-order accurate.

The use of a 7×3 or 3×7 stencil for the HF calculation is obviously arbitrary, although it is the size used previously [1, 3, 5]. However, for this simple problem, we ran the same calculation with smaller stencils (5×3 or 3×5, and 3×3). The use of a 5×3 or 3×5 stencil yielded identical results as for the 7×3 or 3×7, as the sessile drop is well resolved even at $\Delta=\frac{1}{64}$. However, using a 3×3 stencil, the results were dramatically different: the normals were reasonably accurate at coarse resolutions, but did not converge appreciably with refinement; and the curvatures were very inaccurate, and errors actually increased with refinement.

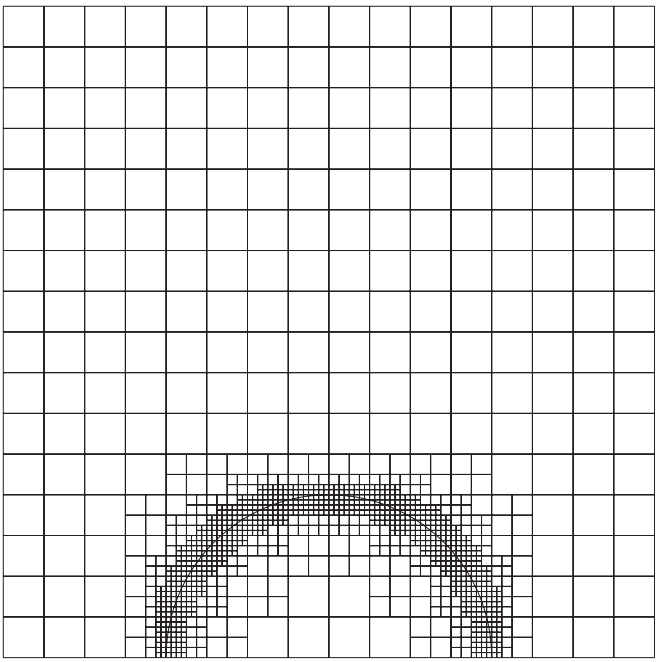

Figure 5. The adaptive mesh associated with a semicircular drop, $\theta=90°$.

DOI: 10.1002/fld

Table I. L_∞ error norms for normals and curvatures, for a semicircular drop initialized exactly, θ = 90°.

	HF		$\nabla \tilde{f}$	
Δ	$\hat{n}$	κ	$\hat{n}=\nabla\tilde{f}/\lvert\nabla\tilde{f}\rvert$	$\kappa=-\nabla\cdot\hat{n}$
$\frac{1}{64}$	0.0198	0.0500	0.0165	0.5964
$\frac{1}{128}$	0.0098	0.0130	0.0175	1.5504
$\frac{1}{256}$	0.0049	0.0030	0.0183	3.1786

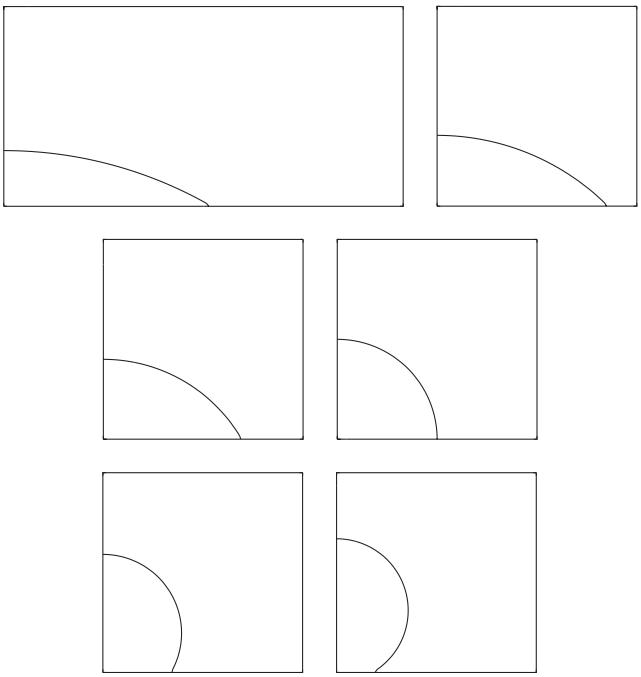

Figure 6. Drops in equilibrium for $\theta=30$, 45, 60, 90, 120, and 150°. Owing to symmetry, only half of the domain is modelled.

3.2. Drops in equilibrium

Next we consider sessile drops, for contact angles that vary from 30 to 150° (Figure 6), in the absence of gravity. For all cases, the drop volume is the same, equal to that of a semicircle of $R=0.5$. The exact interface profiles are circular arcs defined by the given contact angle; the initial volume fractions were computed to machine precision. This set of tests can be thought of as the equivalent of the 'static drop' test utilized by many authors to assess implementations of surface tension without contact lines. The expectation is that a drop initially at rest will remain so; here we expect the sessile drops to behave similarly.

DOI: 10.1002/fld

Table II. The effect of Δt on L_1 and L_∞ norms of spurious velocities, for a drop in equilibrium, $\theta = 60°$, $\Delta = \frac{1}{64}$.

Δt	$\tau = 1$	$\tau = 10$	$\tau = 20$
L_1			
20×10^{-4}	2.31E−8	1.74E−7	3.07E−7
10×10^{-4}	2.43E−8	1.71E−7	3.04E−7
5×10^{-4}	3.03E−8	1.83E−7	3.02E−7
L_∞			
20×10^{-4}	1.44E−6	9.62E−7	1.03E−6
10×10^{-4}	1.44E−6	9.56E−7	1.03E−6
5×10^{-4}	1.45E−6	9.55E−7	1.02E−6

Table III. L_1 and L_∞ norms of spurious velocities as a function of mesh refinement, for a drop in equilibrium, $\theta = 60°$, $\Delta t = 10^{-3}$.

Δ	$\tau = 10$	$\tau = 50$	$\tau = 100$
L_1			
$\frac{1}{32}$	7.44E−7	1.84E−6	1.01E−6
$\frac{1}{64}$	1.71E−7	4.22E−7	2.19E−7
$\frac{1}{128}$	3.92E−8	1.02E−7	1.07E−7
L_∞			
$\frac{1}{32}$	3.69E−6	5.69E−6	2.32E−6
$\frac{1}{64}$	9.54E−7	1.45E−6	4.79E−7
$\frac{1}{128}$	2.44E−7	3.29E−7	2.48E−7

Table IV. L_1 and L_∞ error norms for volume fractions f as a function of mesh refinement, for a drop in equilibrium, $\theta = 60°$, $\Delta t = 10^{-3}$.

Δx	$\tau = 10$	$\tau = 50$	$\tau = 100$
L_1			
$\frac{1}{32}$	5.23E−6	6.27E−5	7.61E−5
$\frac{1}{64}$	1.20E−6	1.48E−5	1.80E−5
$\frac{1}{128}$	2.50E−7	3.37E−6	4.22E−6
L_∞			
$\frac{1}{32}$	8.17E−4	4.65E−3	5.89E−3
$\frac{1}{64}$	4.89E−4	2.50E−3	3.22E−3
$\frac{1}{128}$	2.73E−4	1.20E−3	1.59E−3

DOI: 10.1002/fld

Table V. L_1 and L_∞ norms of spurious velocities when the exact curvature $(1/R)$ is imposed, for a drop in equilibrium, $\theta=60°$, $\Delta=\frac{1}{64}$, $\Delta t=10^{-3}$.

$\tau=10$	$\tau=50$	$\tau=100$
L_1		
1.56E−10	2.39E−10	3.39E−10
L_∞		
8.06E−10	1.16E−9	9.39E−10

The domain size was 1×1 for $45°\leqslant\theta\leqslant150°$, and 2×1 for $\theta=30°$. Only half of a droplet was modelled; a symmetry boundary condition was applied at the left side of the domain. Open boundary conditions were applied at the right and top sides, and a no-slip condition was imposed at the solid boundary on the bottom. The properties of water and air were used for all of the calculations. The relevant non-dimensional quantity is the Ohnesorge number $Oh=\mu_w/\sqrt{\sigma\rho_w D}$, which is the ratio of the viscous force to the surface tension force; D is the drop diameter and the subscript w refers to water. For $\theta=30$, 45, 60, 90, 120, and 150°, the corresponding Ohnesorge numbers are $Oh\approx5.8\times10^{-3}$, 7.8×10^{-3}, 9.5×10^{-3}, 1.2×10^{-2}, 1.3×10^{-2}, and 1.4×10^{-2}, respectively.

We first present a convergence study based on the results for $\theta=60°$. We ran a set of computations at various mesh resolutions ($\Delta=\frac{1}{32}$, $\frac{1}{64}$, and $\frac{1}{128}$) and time steps ($\Delta t=20\times10^{-4}$, 10×10^{-4}, and 5×10^{-4}). We determined the mean and maximum spurious velocities induced in the domain, and then examined the effect of these velocities on how far the droplets deviated from the known equilibrium positions, as measured by differences in volume fractions f:

$$L_1=\sum_{i=1}^{N}|f_{i,\text{exact}}-f_i|\Delta_i^2 \tag{21}$$

$$L_\infty=\max|f_{i,\text{exact}}-f_i| \tag{22}$$

Note that the definition of L_1 includes Δ_i; the subscript i reflects the fact that the mesh is adaptive, even though all interface cells are of size Δ. N is the number of cells in the domain.

Norms of mean and maximum spurious velocities, and f error norms, are presented in Tables II–IV. Table II presents the effect of Δt on spurious velocities, with $\Delta=\frac{1}{64}$, at different non-dimensional times $\tau=t\sigma/(\mu D)$. The spurious velocities grow with time, but are very small and largely independent of Δt. Based on these results, $\Delta t=10^{-3}$ was chosen for all subsequent simulations; note that this Δt is well below the capillary time step constraint [7].

Table III presents the convergence behaviour of spurious velocities and Table IV the corresponding f errors, as a function of mesh size, each at several times τ. For the most part, the norms of spurious velocities diminish at a second-order rate with mesh refinement; the norms for $\Delta=\frac{1}{64}$ and $\frac{1}{128}$ at $\tau=100$ are an anomaly, presumably because the norms of the spurious velocities oscillate somewhat in time. The f errors presented in Table IV diminish more clearly at a second-order rate. Overall, these results demonstrate that when normals and curvatures are calculated *via* HFs, these contact line calculations converge.

For comparison, Table V presents the norms of spurious velocities when the exact curvature is prescribed, for $\Delta=\frac{1}{64}$. These values are three orders of magnitude less than the corresponding

DOI: 10.1002/fld

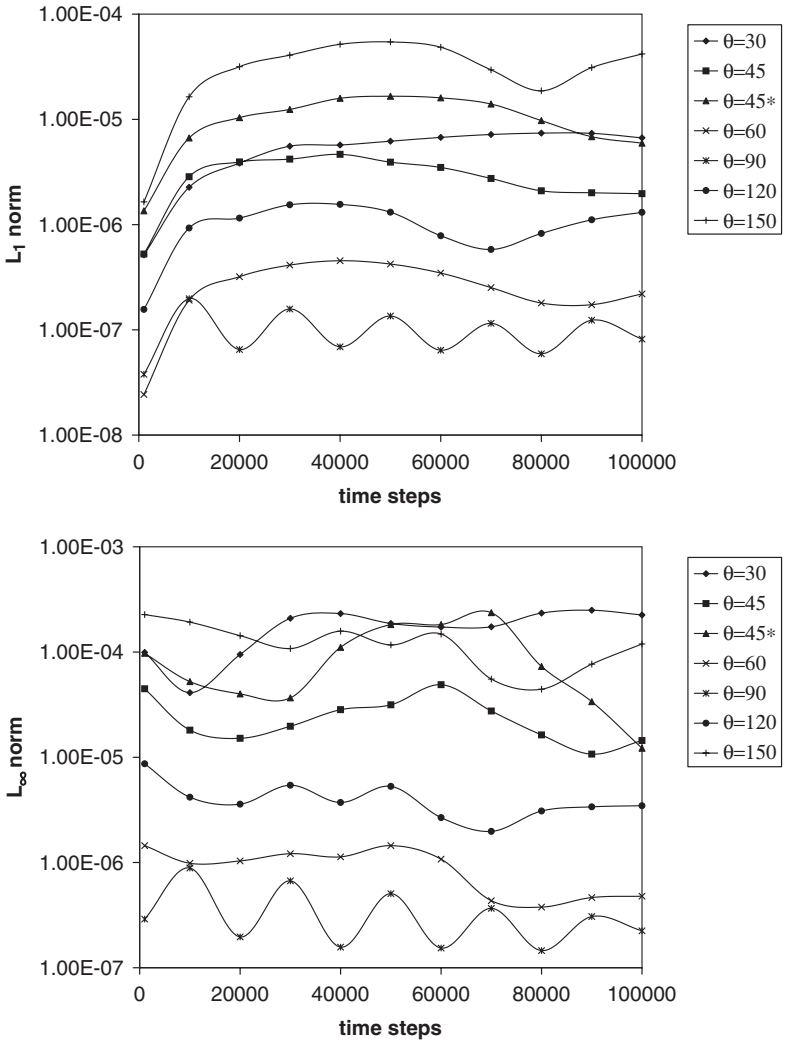

Figure 7. L_1 and L_∞ norms of spurious velocities *versus* the number of time steps, for $\Delta = \frac{1}{64}$, $\Delta t = 10^{-3}$. Note that $\theta = 45^*$ indicates the use of vertical heights at the contact line.

values of Table II, and evidence the consistent approach used to discretize F_{st} and ∇p. The reason these norms are not exactly zero is due to the tolerance (10^{-6}) specified for the iterative pressure Poisson solver. Nevertheless, Table V clearly shows the extent to which the velocities of Table III originate from the curvature calculation.

We now present results for $\theta = 30$, 45° (calculated using both horizontal and vertical HFs), 60, 90, 120, and 150°, with $\Delta = \frac{1}{64}$ and $\Delta t = 10^{-3}$. Figure 7 illustrates the evolution of spurious currents with respect to time: the norms of these velocities quickly asymptote, albeit to values that are a function of θ. The corresponding errors in volume fractions are shown in Figure 8. Here, we

DOI: 10.1002/fld

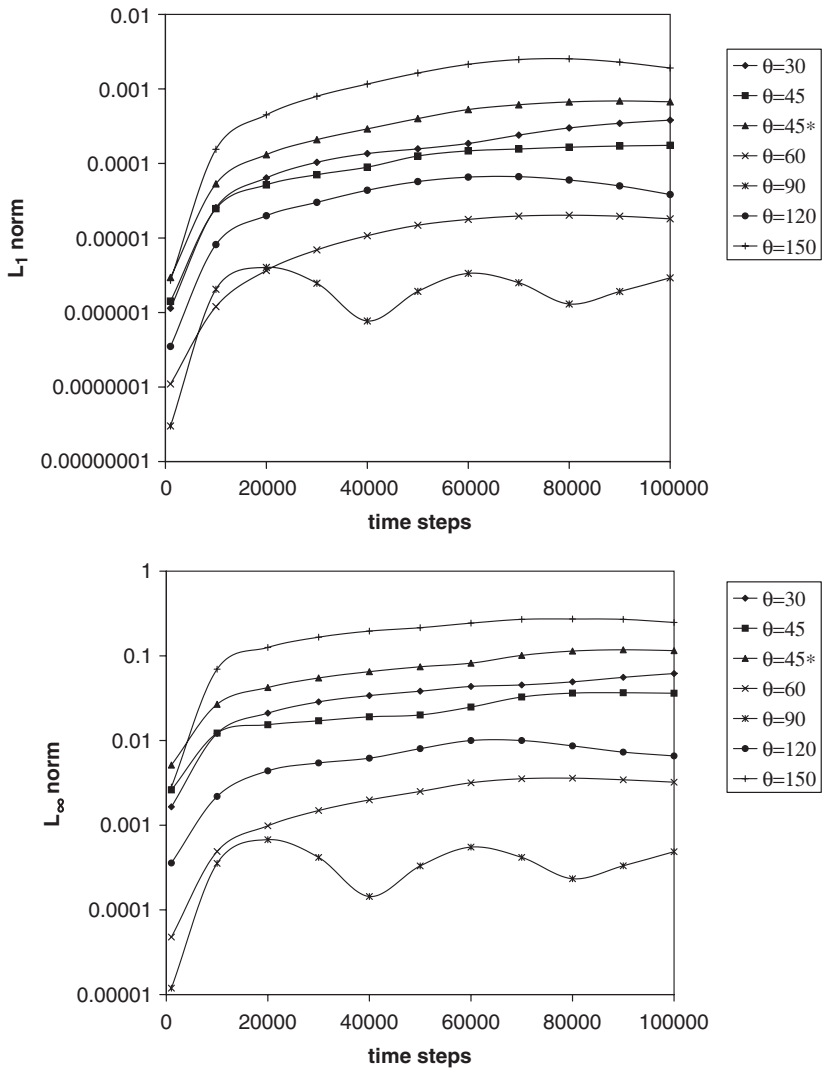

Figure 8. L_1 and L_∞ error norms for volume fractions f *versus* the number of time steps, for $\Delta = \frac{1}{64}$, $\Delta t = 10^{-3}$. Note that $\theta = 45^*$ indicates the use of vertical heights at the contact line.

also observe that the errors asymptote to maximum values, although more slowly than the spurious currents, which are driving the fluctuations in f.

There are two reasons for the significant variation in the magnitude of spurious currents and f errors as a function of θ. First, the variations are roughly proportional to errors in calculated contact line curvatures. For $\theta = 90°$, which corresponds to a symmetry condition for f at the solid surface, contact line curvatures are as accurate as curvatures calculated anywhere else in the domain. For $\theta = 60$ and $120°$, the linear extrapolation of a horizontal fluid height into the ghost cells (Equation (19)) affects the calculated contact line curvatures, although these values are still very

DOI: 10.1002/fld

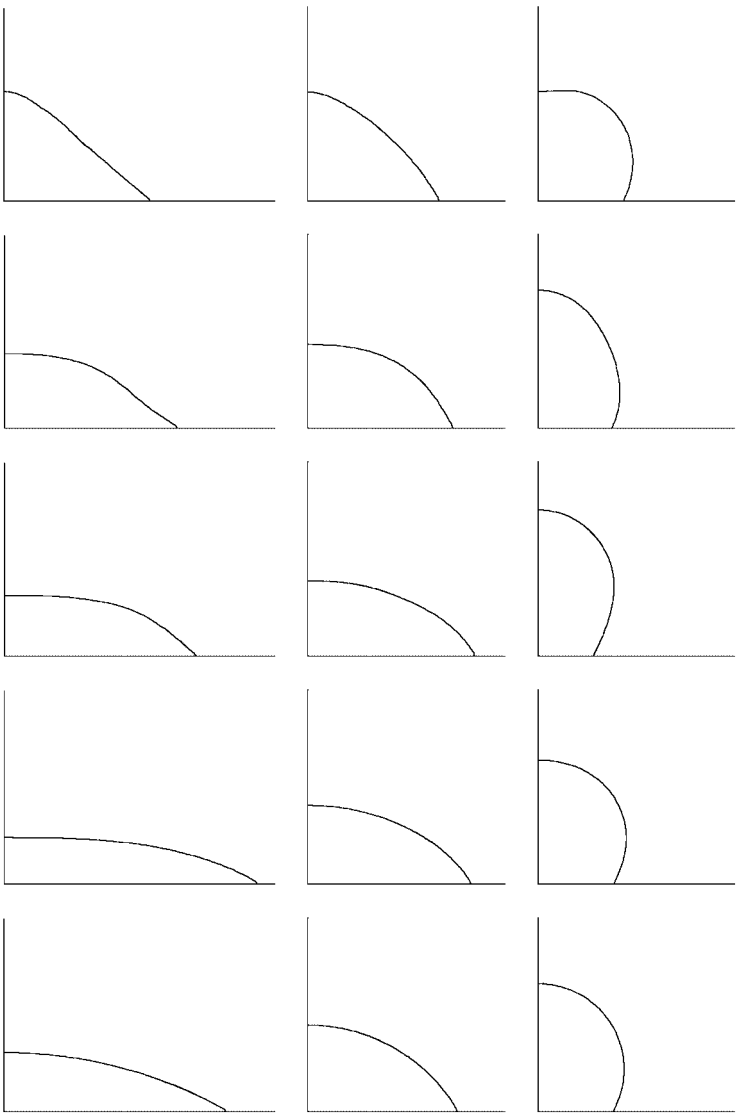

Figure 9. Profiles of an initially semicircular drop to which contact angles $\theta = 30°$ (left), 60° (middle), and 120° (right) are suddenly applied; results at non-dimensional times $\tau = 40$, 50, 60, 110, and 1600 (top to bottom); $\Delta = \frac{1}{64}$, $\Delta t = 10^{-3}$.

accurate. For $\theta = 30$ and 150°, the contact line curvatures are based on two linearly extrapolated values, the vertical heights h_i and h_{i-1} illustrated in Figure 4; these curvatures are then not as accurate as those calculated from horizontal HFs. To further demonstrate the difference between horizontal and vertical HFs, we ran the case of $\theta = 45°$ both ways. As Figures 7 and 8 illustrate, the use of horizontal HFs yielded spurious velocities and f errors about an order of magnitude lower than corresponding results obtained *via* vertical HFs.

DOI: 10.1002/fld

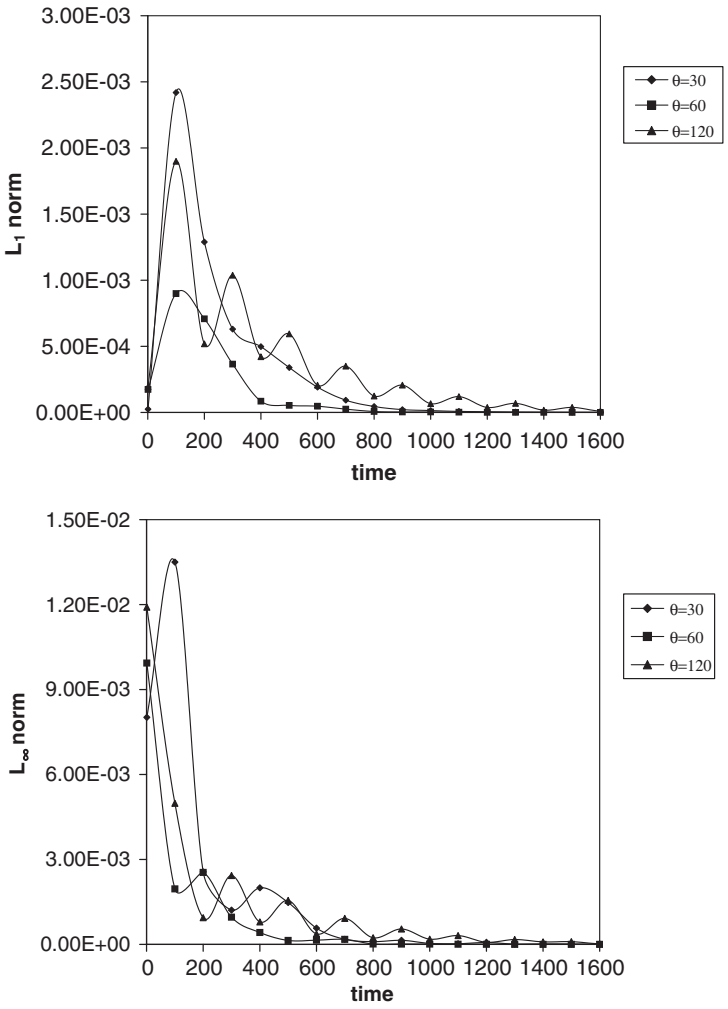

Figure 10. Mean and maximum velocities as an initially semicircular drop evolves to a steady state defined by $\theta = 30$, 60, and 120°; $\Delta = \frac{1}{64}$, $\Delta t = 10^{-3}$.

The second reason for the variation of spurious currents and f errors is related to the effective length of the contact line, which varies inversely with θ because the drop volume is the same for all cases. Thus, results for $\theta = 60°$ are more accurate than those for $\theta = 120°$, because the $\theta = 60°$ contact line is better resolved, everything else being equal; the same argument explains why the $\theta = 30°$ results are more accurate than those for $\theta = 150°$. Having said that, note that the norms of f errors presented in Figure 8 are very small. At worst ($\theta = 150°$), the maximum deviation of f from an exact value is about 0.1, which corresponds to a deviation in interface position of about $\Delta/10$. The average deviation is orders of magnitude smaller, as are the deviations associated with other values of θ.

DOI: 10.1002/fld

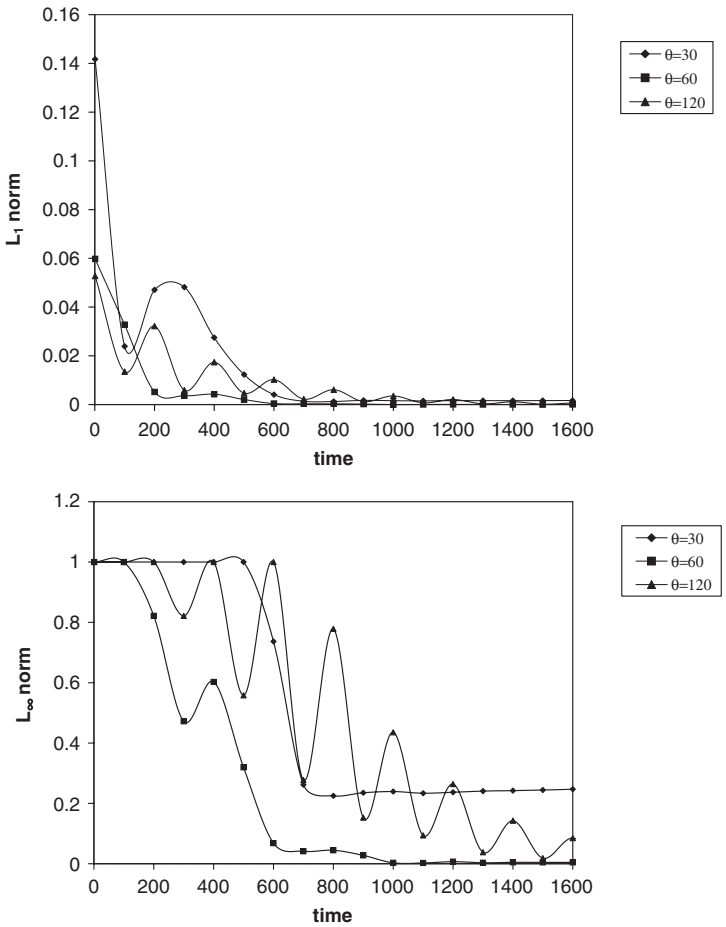

Figure 11. The average and maximum differences between calculated interface profiles and the known equilibrium configurations, as a function of non-dimensional time; $\Delta = \frac{1}{64}$, $\Delta t = 10^{-3}$.

3.3. Contact line-driven flows

Finally, to illustrate the overall performance of the methodology on problems that involve appreciable flow, we present results of flow driven by the contact line. Of interest is the evolution of a drop to a new equilibrium position due to a sudden change in the contact angle boundary condition. Consider again the configuration of Figure 5. In the absence of gravity, the drop as illustrated is in equilibrium if $\theta = 90°$. If at $t = 0$ the value of θ suddenly changes, then the droplet should move towards a circular shape defined by the new contact angle. For the properties of water and air (density ratio of 10^3, viscosity ratio of 10^2), the Ohnesorge number is $Oh = 1.2 \times 10^{-2}$. The drop volume, domain and mesh size, and boundary conditions are the same as those in Section 3.2. Regarding mass conservation of the volume tracker in these cases, a comparison of the initial and final total fluid volumes showed differences in the range of 0.001–0.00001%.

DOI: 10.1002/fld

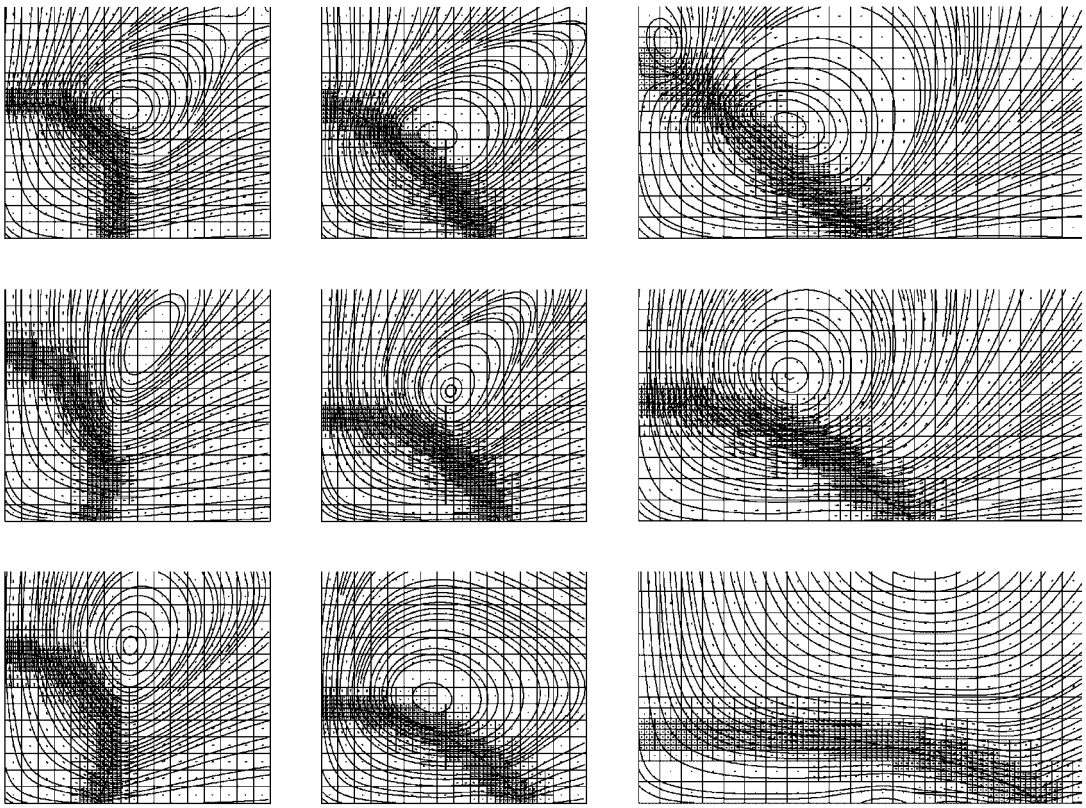

Figure 12. Velocity fields at non-dimensional times $\tau = 20$, 40, and 110 (top to bottom), as semicircular drops move towards equilibrium states defined by $\theta = 120$, 60, and 30° (left to right).

Figure 9 illustrates the flow of an initially semicircular drop to three new equilibrium positions corresponding to $\theta = 30$, 60, and 120°. (We do not present results for $\theta = 150°$ because this large value of θ leads to the droplet pinching off of the solid surface; in the absence of gravity, the droplet does not return to the surface.) We ran the simulations to steady state, when the velocities in the domain approached values similar to the spurious velocities encountered in the results of Section 3.2. Figure 10 shows the mean and maximum velocities as a function of time: the sudden change in θ at $t = 0$ induces a sudden increase in the velocities that is followed by oscillations as the interface settles into its equilibrium position. Figure 11 shows the deviation between the calculated interface and the final equilibrium configurations, as measured by the norms defined by Equations (21) and (22). Obviously, the L_∞ deviation is 1 at the beginning, as the initial and equilibrium shapes are quite different, but Figure 11 does illustrate that the droplets reach equilibrium positions that are nearly as accurate as those presented in Section 3.2.

Finally, Figure 12 illustrates the flow fields about these contact line-driven drops, at different times τ. In particular, the streamlines clearly depict the vortices induced in the air above the droplets, as the droplets evolve to their equilibrium positions, and the dissipation of the vortices at later times ($\tau = 110$), as the droplets approach their final positions.

DOI: 10.1002/fld

4. SUMMARY

The accurate evaluation of surface tension has been a long-standing challenge for the VOF methodology. Recent work has demonstrated a consistent approach to applying the surface tension force, and better approaches to calculating normals and curvatures, that we have incorporated into an adaptive VOF-based interfacial flow solver, and extended for the accurate evaluation of surface tension at 2D contact lines. We demonstrated the accuracy and the convergence behaviour of normals and curvatures calculated *via* HFs at the contact line, the magnitude of the spurious currents that arise from simulations of interfacial phenomena in equilibrium, and results of contact line-driven phenomena that demonstrate the efficacy of the methodology. We believe this work is a step towards development of more sophisticated 2D and 3D contact line models.

REFERENCES

1. Cummins SJ, Francois MM, Kothe DB. Estimating curvature from volume fractions. *Computers and Structures* 2005; **83**:425–434.
2. Gerlach D, Tomar G, Biswas G, Durst F. Comparison of volume-of-fluid methods for surface tension-dominant two-phase flows. *International Journal of Heat and Mass Transfer* 2006; **49**:740–754.
3. Francois MM, Cummins SJ, Dendy ED, Kothe DB, Sicilian JM, Williams MW. A balanced-force algorithm for continuous and sharp interfacial surface tension models within a volume tracking framework. *Journal of Computational Physics* 2006; **213**:141–173.
4. Renardy Y, Renardy M. A parabolic reconstruction of surface tension for the volume-of-fluid method. *Journal of Computational Physics* 2002; **183**:400–421.
5. Sussman M. A second order coupled level set and volume-of-fluid method for computing growth and collapse of vapor bubbles. *Journal of Computational Physics* 2003; **187**:110–136.
6. Renardy M, Renardy Y, Li J. Numerical simulation of moving contact line problems using a volume-of-fluid method. *Journal of Computational Physics* 2001; **171**:243–263.
7. Brackbill JU, Kothe DB, Zemach C. A continuum method for modeling surface tension. *Journal of Computational Physics* 1992; **100**:335–354.
8. Kothe DB, Mjolsness RC. RIPPLE: a new model for incompressible flows with surface tension. *AIAA Journal* 1992; **30**:2694–2700.
9. Pasandideh-Fard M, Qiao YM, Chandra S, Mostaghimi J. Capillary effects during droplet impact on a solid surface. *Physics of Fluids* 1996; **8**:650–659.
10. Bussmann M, Mostaghimi J, Chandra S. On a three-dimensional volume tracking model of droplet impact. *Physics of Fluids* 1999; **11**:1406–1417.
11. Liu H, Lavernia EJ, Rangel RH. Modeling of molten droplet impingement on a non-flat surface. *Acta Metallurgica et Materialia* 1995; **43**:2053–2072.
12. Lafaurie B, Nardone C, Scardovelli R, Zaleski S, Zanetti G. Modelling merging and fragmentation in multiphase flows with SURFER. *Journal of Computational Physics* 1994; **113**:134–147.
13. Scardovelli R, Zaleski S. Direct numerical simulation of free-surface and interfacial flow. *Annual Review of Fluid Mechanics* 1999; **31**:567–603.
14. Youngs DL. Time-dependent multi-material flow with large fluid distortion. In *Numerical Methods for Fluid Dynamics*, Morton K, Baines M (eds). Academic Press: New York, 1982; 273–285.
15. Pilliod Jr JE, Puckett EG. Second-order accurate volume-of-fluid algorithms for tracking material interfaces. *Journal of Computational Physics* 2004; **199**:465–502.
16. Kleefsman KMT, Fekken G, Veldman AEP, Iwanowski B, Buchner B. A volume-of-fluid based simulation method for wave impact problems. *Journal of Computational Physics* 2005; **206**:363–393.
17. Veldman AEP, Gerrits J, Luppes R, Helder JA, Vreeburg JPB. The numerical simulation of liquid sloshing on board spacecraft. *Journal of Computational Physics* 2007; **224**:82–99.
18. Hirt CW, Nichols BD. Volume of fluid (VOF) method for the dynamics of free boundaries. *Journal of Computational Physics* 1981; **39**:201–225.
19. Popinet S. The Gerris flow solver. http://gfs.sourceforge.net.

DOI: 10.1002/fld

20. Popinet S. Gerris: a tree-based adaptive solver for the incompressible Euler equations in complex geometries. *Journal of Computational Physics* 2003; **190**:572–600.
21. Almgren AS, Bell JB, Collela P, Howell LH, Welcome ML. A conservative adaptive projection method for the variable density incompressible Navier–Stokes equations. *Journal of Computational Physics* 1998; **142**:1–46.
22. Gueyffier D, Nadim A, Li J, Scardovelli R, Zaleski S. Volume-of-fluid interface tracking with smoothed surface stress methods for three-dimensional flows. *Journal of Computational Physics* 1998; **152**:423–456.
23. Aleinov I, Puckett EG. Computing surface tension with high-order kernels. In *Proceedings of the 6th International Symposium on Computational Fluid Dynamics*, Lake Tahoe, CA, U.S.A., Oshima K (ed.), 1995.
24. Huh C, Scriven LE. Hydrodynamic model of steady movement of a solid/liquid/fluid contact line. *Journal of Colloid and Interface Science* 1971; **35**:85–101.
25. Hocking LM. Sliding spreading of thin two-dimensional drops. *Quarterly Journal of Mechanics and Applied Mathematics* 1981; **34**:37–55.
26. Cox RG. The dynamics of the spreading of liquids on a solid surface. Part 1. Viscous flow. *Journal of Fluid Mechanics* 1986; **168**:169–194.
27. Fukai J, Zhao Z, Poulikakos D, Megaridis CM, Miyatake O. Modeling of the deformation of a liquid droplet impinging upon a flat surface. *Physics of Fluids A* 1993; **5**:2588–2599.

DOI: 10.1002/fld